On avalanche measurements at the Norwegian full-scale test-site Ryggfonn

Peter Gauer [a,b,*], Karstein Lied [a], Krister Kristensen [a]

[a] *Norwegian Geotechnical Institute, Sognsveien 72, NO-0806 Oslo, Norway*
[b] *International Centre for Geohazards, c/o NGI, Norway*

Abstract

Avalanche measurements and observations, which were carried out at the Ryggfonn test-site, Norway, on 16 April 2005, are analyzed. The data include pulsed Doppler radar measurements, impact pressure readings from load cells mounted at two locations within the track and stress readings from load plates flush with the upstream slope of a catching dam. The radar measurements are used to deduce velocities and estimates on the retarding accelerations. The retarding accelerations show a wide discrepancy with commonly used model assumptions. Pressure measurements were correlated with velocity measurements. The measurements infer that commonly used drag factors are not sufficient to describe the forces exerted by slow moving wet snow. These measurements also depict transitions in the flow behavior. Measurements with load plates imply plastic failure rather than Coulomb-type friction. Field observations of the avalanche track suggest that erosion/abrasion due to (saltating) particles is one possible entrainment mechanism.
© 2007 Elsevier B.V. All rights reserved.

1. Introduction

There are only a few dedicated full-scale avalanche test-sites; full-scale avalanche in the sense that avalanches of size 4 and more according to the Canadian avalanche size classification (McClung and Schaerer, 1993) could be observed. Probably, one of the first sites was the Russian site at Khibini (cf. Kotlyakov et al., 1977; Bozhinskiy and Losev, 1998). Certainly, also the measurements at Rogers pass belong in the line of early full-scale measurements (McClung and Schaerer, 1985; Schaerer and Salway, 1980). The Ryggfonn site is operated by the Norwegian Geotechnical Institute since the early 1980s. First measurements from this site can be found in Norem et al. (1985) and Bakkehøi et al. (1983). In Japan, the Kurobe Canyon serves as an instrumented full-scale test-site (Kawada et al., 1989; Nishimura et al., 1989, 1993). Since Winter 1997/1998, the Swiss test side Vallée de la Sionne/Valais is in full operation (Ammann, 1999). However, also its predecessor should be mentioned, although, mostly only radar measurements were performed at Lukmanier Pass, Val Medel/Grisons (Gubler, 1987; Salm and Gubler, 1985).

In the previous paragraph, we took the size 4 avalanche as a "limit" for the definition of full-scale test-

* Corresponding author. Norwegian Geotechnical Institute, P.O. Box 3930 Ulleval Stadion, NO-0806 Oslo, Norway. Tel.: +47 22 02 31 29; fax: +47 22 23 04 48.

E-mail address: pg@ngi.no (P. Gauer).

sites, as avalanches of this size and larger form the devastating avalanches most relevant in respect to hazard zoning. Although, a size 3 can also destroy a small building. There are a couple of smaller test-sites focusing on smaller size natural avalanches. Those sites are of importance, as they narrow the gap between small-scale laboratory experiments and the aforementioned full-scale sites providing valuable insight to avalanche dynamics. A comprehensive overview of the (European) avalanche test-sites can be found in Issler (1999), and an updated version of it in Barbolini and Issler (2006).

Although measurements of full-scale avalanches are expensive and time consuming, and are difficult to perform under those harsh conditions within an avalanche (and not always easy to understand), they are indispensable to gain in-depth understanding of the flow behavior of avalanches. They are needed to cross-check the scaling used in small-scale experiments. They also form the basis for developing and calibrating models. Information on experimental techniques and sensors can be found in Issler (2003).

In the following, we summarize measurements and observations from one full-scale event (20050416 15:00) at Ryggfonn and give some interpretations of those measurements. Although we focus on this single event, a few measurements from two other events are also briefly discussed at one point to give some cross comparison.

2. Ryggfonn test-site

The Norwegian Geotechnical Institute (NGI) has been operating the full-scale avalanche test-site Ryggfonn in Western Norway for more than 25 years. The test-site is characterized by a north facing bowl in the upper part of the track, a vertical drop of about 900 m in total, and a maximum horizontal path length of up to 2100 m. The mean inclination of the main track is about 29°. Typical avalanche sizes range between 2 (mass of 10^5 kg) and 4 (mass of 10^7 kg), and may even reach class 5, according to the Canadian snow avalanche size classification. Maximum observed front velocities are as high as 60 m s^{-1}. Observations include dry and wet snow avalanches. Fig. 1 gives an overview of the test-site.

During the years, the instrumentation has changed. At present, measurements from Ryggfonn avalanche test-site include pressure readings from five load cells, each being 1.2×0.6 m^2 in size, installed at two locations in the lower third of the track; three are attached to a concrete wedge and two to a steel tower. The load cells
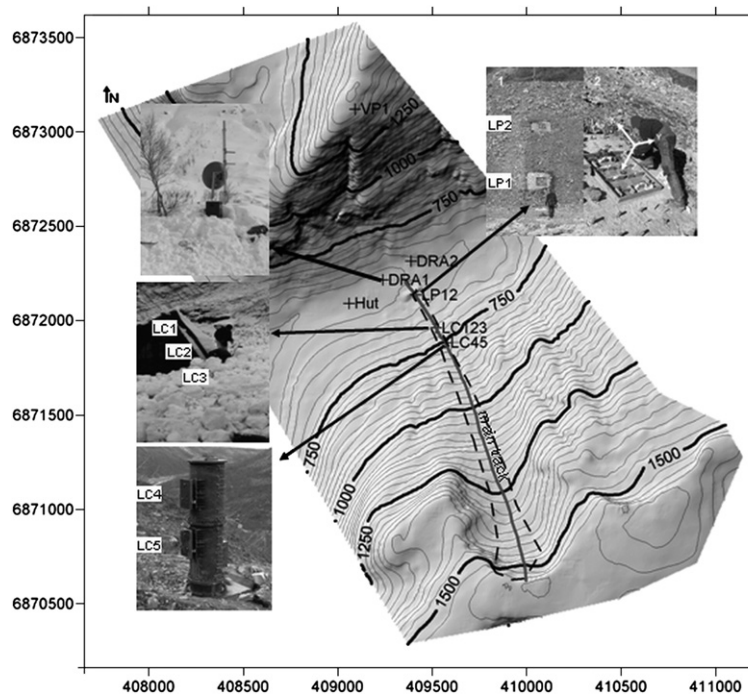

Fig. 1. Overview of the Ryggfonn test-site. The view shows the line of the main path, the locations of the load cells (LC45 and LC123) and the placement of the load plates in the dam (LP1 and LP2). In addition, two Doppler radar positions are indicated (DRA1 and DRA2). The dashed line indicates the outline of the 20050416 15:00 event. Coordinates are UTM and isolines are 25 m apart.

LC3, LC2, and LC1 are mounted such that the vertical heights of the respective midpoint are approximately 0.5 m, 1.5 m, and 2.5 m above ground. The load plates are inclined by 30° as such they are nearly perpendicular to the local slope. At the steel tower, the mid point of LC5 and LC4 is 2.25 m and 4.25 m above foundation level, respectively. From a dynamic point of view, the load cells are regarded as rectangular bodies (plates). At a 16 m high catching dam in the runout zone, normal and shear stresses are measured at two places using load plates with a size of 1×1 m^2. The load plates are mounted flush with the upstream slope of the dam at vertical heights of 2 and 8 m above the base measuring the three stress components: (z) normal to the slope, (x) shear pointing towards the dam crown and (y) shear pointing at a right angle. All load cells and load plates are constructed of strain-gauge devices.

The crown length of the dam is 75 m and dam slope is between 35 and 40°. In addition, six geophones are placed in the ground in the runout zone. Recently, two pairs of FMCW Doppler radar were also buried in the lower part of the track. These should provide information on flow height, erosion, and, hopefully, on the vertical velocity profile. Additionally, NGI owns a pulsed Doppler radar for velocity measurements along the path. Exploiting the Doppler effect, a pulse Doppler radar makes it possible to gain information on the front speed along the path and information on the velocity vs. time at specific locations along the path.

3. Measurements and observations

On 16 April 2005 a size 4 avalanche was released by detonating 150 kg of explosives buried in the top cornice at the ridge line above the bowl. Preceding the event were nearly 2 months of stable weather and snow conditions. The first part of April showed a period of snowfall and south-westerly winds favoring blowing and drifting snow. Around the 15th, the weather cleared and at the same day a small avalanche ran in the lower path as a result of the afternoon sunshine.

On the following day, the weather during the release was sunny and calm with 0.25 m fresh snow deposited from the previous days. At 1420 masl, the air temperature was -2.5 °C with high temperatures of -1.5 °C in the preceding 24 h. South-westerly winds blew at 2 m s^{-1} with gusts up to 5 m s^{-1}. In the runout zone the air temperature reached about 5 °C at the time of release.

The avalanche started out as a dry-mixed one. At the end of the bowl, it nearly came to halt, but it picked up some speed again in the steeper lower section of the track. There, it eroded a substantial amount of snow and probably triggered a second wet slide. The approximated outline of the avalanche is shown in Fig.1. Table 1 gives a characterization of the event following the Canadian size classification (cf. McClung and Schaerer, 1993) and the International Avalanche Classification (Avalanche Atlas, UNESCO, 1981). In addition, the classification of two other avalanches is given for which pulsed Doppler radar data were available and which are briefly discussed in Section 3.2.

3.1. Velocity measurements

Velocity was measured using a pulsed Doppler radar with a signal frequency of 5.8 GHz. Echo signals in this frequency range originate mainly from within the fluidized (saltation) layer or the upper-surface of the dense flow and therefore, give information on the velocity of the so-called flowing part of an avalanche. A Doppler radar as such exploits the apparent frequency shift of the reflected radar signal due to the motion of targets relative to the radar yielding in a velocity distribution/spectrum within the width (volume) covered by a range gate, i.e., a spatial window in the direction of the radar beam. The reflected echo power intensity is an indicator for the size of coherently moving target. Pulsed Doppler radar measurements do not provide any information on the vertical velocity profile. However, in contrast to single point measurements at a pylon within the track, they provide information on the velocity development of the avalanche along the path, e.g., information on the front velocity and time series of the velocity at several locations along the path covered by the respective range gate. Radar measurements are nonintrusive. Using those velocity data, it is possible to gain an estimate on retarding accelerations. The retarding acceleration is a measure for the resisting forces acting on an avalanche. A detailed description on the radar measurements as such and the deduction of

Table 1
Avalanche characterization

Date	Size	Classification (ICSI)								
yyyymmdd hh:mm		A	B	C	D	E	F	G	H	J
19970417 14:00	3	2	2	1	2	7	3	7	1	4
20030406 13:06	2/3	3	2	1	2	7	3	1	1	4
20050416 15:00	4	4	7	1	2	7/2	3	7	3	4

The avalanche event 20050416 15:00 is also documented in Gauer and Kristensen (2005); the event 20030406 13:06 in Gauer and Kristensen (2004) and the 19970417 14:00 event in Schreiber et al. (2001) and Rammer et al. (1998).

accelerations a can be found in (Gauer et al., 2007). The paper also contains a discussion on the error estimates.

During 20050416 15:00 event, it was possible to gain pulsed Doppler radar measurements from the lower part of the track (below about 800 masl). Fig. 2 shows two examples of the measured velocity spectra given by its power echo intensity and the velocity of the maximum intensity The data originate from range gates RG19 and RG15. RG19 covers the area around the steel tower and RG15 the area around the concrete wedge. The power echo intensity is normalized by its overall maximum of the respective range gate; the relative values are given in the figure. The spectra are rather narrow suggesting a rather coherent motion of the avalanche. In both cases, a branch with lower intensity suggests that parts of the avalanche start to deposit (time, $t < 10$ s). At RG15, two branches can be observed for $t > 22$ s. This indicates that the avalanche split. The slower branch shows the higher
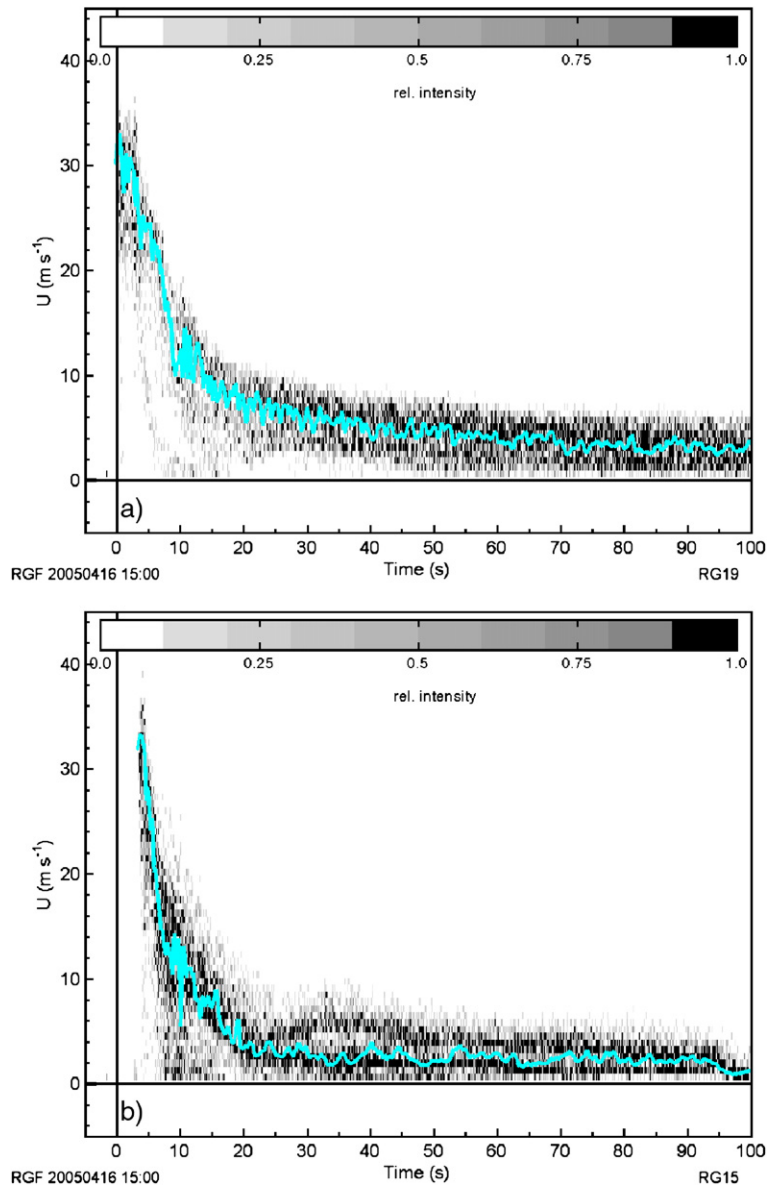

Fig. 2. Avalanche 20050416 15:00: velocity of max power echo intensity vs. time (cyan line). In addition the relative power intensity is shown (grey coded). a) RG19, which covers the area around the steel tower, and b) RG15 covering the concrete wedge. (For interpretation of the references to colour in this figure legend, the reader is referred to the web version of this article.)

echo intensity indicating that this branch is larger. In the present case, the velocity of the maximum intensity is a good approximation for the velocity of the avalanche approaching (closing in upon) the radar position. The estimated error for the present avalanche is around ± 2.5 ms^{-1} based on calculated weighted means and standard deviations not shown here.

Fig. 3 depicts velocity measurements (averaged velocity between two range gates RG(i) and RG($i-1$)) and deduced retarding accelerations for seven instants in time (measured relative to the arrival time at the steel tower). In addition, the front velocity is shown in the upper panel. In the lower panel, the driving (slope parallel) component of the gravity, $a_{\mathrm{slp}} = g$
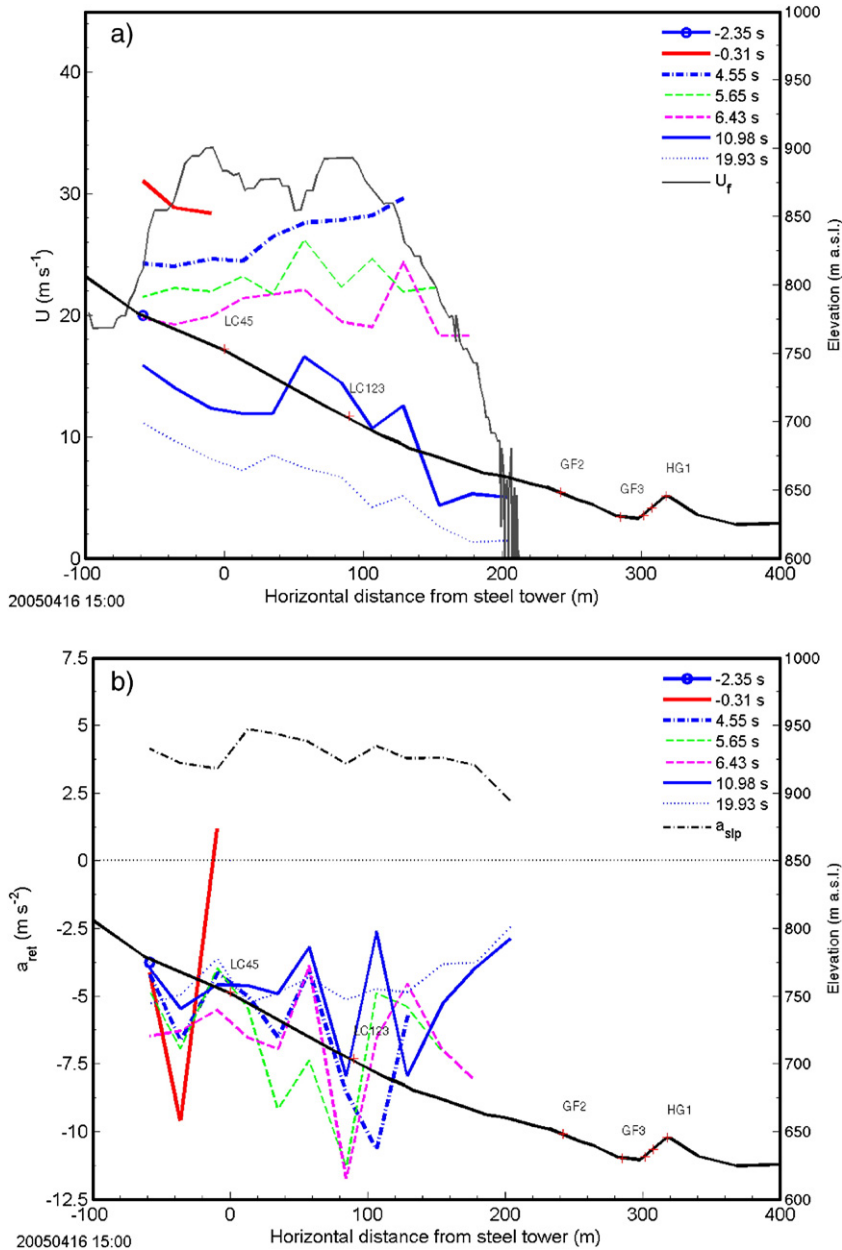

Fig. 3. Avalanche 20050416 15:00: averaged velocity (panel a) and corresponding retarding acceleration (panel b) vs. location along the lower track for seven instants in time. In addition, the thin solid line in panel a) shows the front velocity, U_{f}. The grey dashed-dotted line in panel b) gives $a_{\mathrm{slp}} = g \sin \phi$. The thick solid lines give the path profile in the lower part of the track and runout zone.

sin ϕ, is given. The averaged velocity, U, is calculated from the measured velocity of the maximum intensity:

$$U(t + \Delta t/2) = \frac{U_{RG(i-1)}(t + \Delta t) + U_{RG(i)}(t)}{2}. \qquad (1)$$

Here, $RG(i-1)$ denotes down-slope positioned range gate. Δt is the time a "fictitious mass block" would need to travel the distance L_{RG}, which corresponds to the width of the range gate of the radar. The retarding acceleration, a_{ret}, is calculated by

$$a_{ret} = a - g\sin\phi, \qquad (2)$$

where g is the gravitational acceleration and ϕ the slope angle, a is the effective or apparent acceleration of a part of the avalanche ("fictitious mass block") within the avalanche. It is derived from the measured velocities of the maximum intensity at to adjoining range gates, $U_{RG(i-1)}$ and $U_{RG(i)}$, by

$$a(t + \Delta t/2) = \frac{U^2_{RG(i-1)}(t + \Delta t) - U^2_{RG(i)}(t)}{2L_{RG}}. \qquad (3)$$

At the time the avalanche enters the area covered by the radar, it is accelerating and the velocity of the frontal part increases. The head velocity tends to be higher than that of the body and tail. This can also be seen from the velocity profiles in Figs. 2 and 7. At the position of the concrete wedge, the avalanche starts to decelerate rapidly. Retarding accelerations are as high as approximately 12 m s^{-2} (absolute value). The dry part at the front stopped about 75–100 m before the dam. The wet part continued to flow slowly for approximately another 2 min piling up in front of the dam.

Fig. 4 plots the retarding acceleration vs. velocity for four locations as the avalanche passes by. This is an Eulerian representation, i.e., we "place" us in middle between two adjoining ranges and follow a series of "fictitious mass block" as they pass by. No unambiguous relation between retarding acceleration and velocity is evident. The mean slope angle at the steel tower is approximately 30° and at the concrete wedge about 26°, however, there is a steep step just below the wedge, which depending on the previous snow deposition is more or less evident. The estimated error range of the retarding acceleration is $\pm\Delta a$. The offset in the plot of $\pm\Delta a$ is set to the overall mean of calculated acceleration values.

At low velocities ($\lesssim 10$ m s^{-1}), three of the four plots imply velocity independency. Actually, the word retarding acceleration might be slightly misleading. The retarding acceleration includes contribution of all forces acting on the mass block, except those originating from gravity. Hence, it includes also components from pressure gradient forces, which can cause a positive
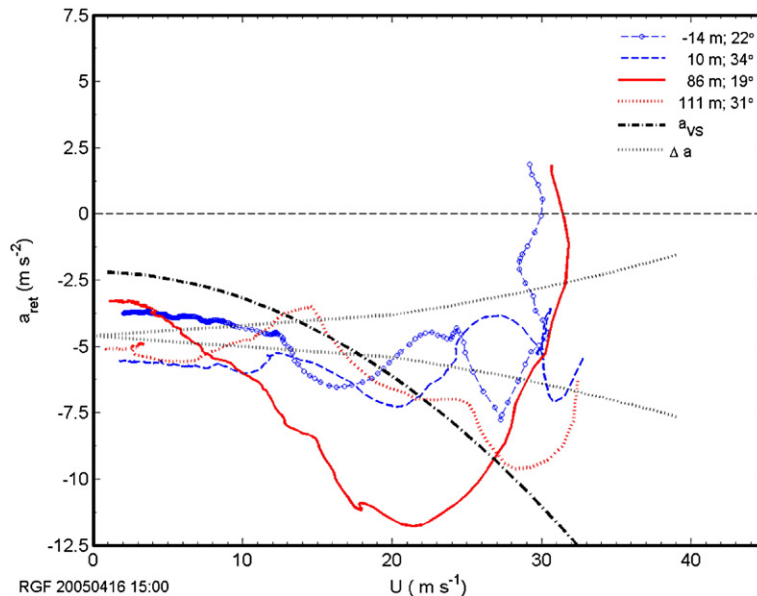

Fig. 4. Avalanche 20050416 15:00: retarding acceleration vs. velocity at four points. The first two correspond to points just above and below the steel tower (LC45) and the other two to points above and below the concrete wedge (LC123). Numbers give the relative position to the steel tower and the mean slope angle at those points. a_{VS} is the retarding component according to Eq. (4). The dashed-dotted grey line marked Δa gives an error estimate on the acceleration.
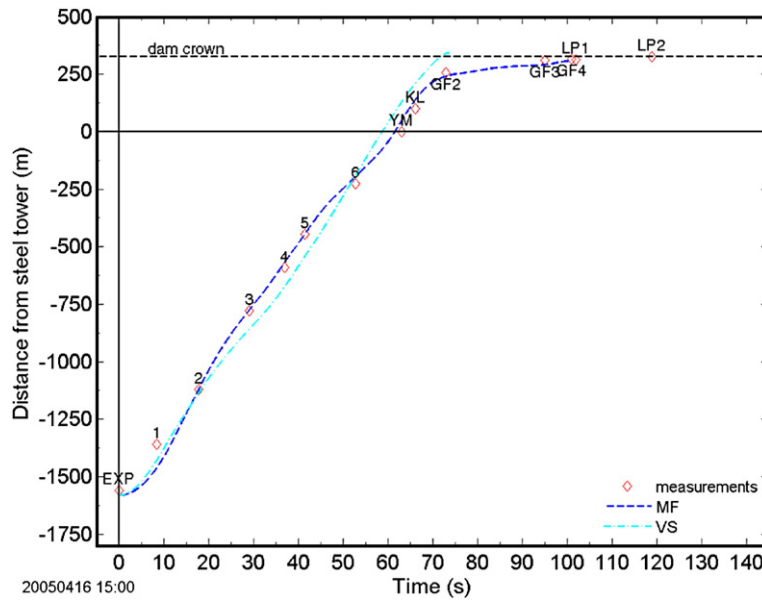
Fig. 5. Avalanche 20050416 15:00: estimated travel distance vs. time derived by a combination of video analysis and arrival time at various sensors. Lines correspond to simple model calculations based on Eq. (5).

acceleration as observed in the figure. We are aware that deducing an acceleration from velocity measurements has its limitations.

In addition to the deduced retarding accelerations, the resistance component as it would be given, e.g., in a Voellmy–Salm type model is also shown in the figure:

$$a_{VS} = -g\left(\mu cos\phi + \frac{u^2}{\xi h_a}\right). \qquad (4)$$

The parameters used are only estimates: $h_a = 1.5$ m, $\mu = 0.25$, and $\xi = 1000$ m s^{-2}. However, the latter two are in accordance to the Swiss guidelines (Salm et al., 1990; Gruber et al., 1999). The assumed slope angle for this example is 26° corresponding to the mean slope angle between the steel tower and concrete wedge. Obviously, the model would underestimate the resistance at low velocities whereas it overestimates it at high speeds.

Unfortunately, there are no radar measurements available in the upper part of the track, however, the evolution of the front velocity could be tracked from video analysis and the arrival time at various sensors. Fig. 5 plots the evolution of the front along the track. It also shows the time evolution for two simple model calculations based on

$$\frac{du}{dt} = g\sin\phi + a_{ret} \qquad (5)$$

where a_{ret} is either given by the VS-type model (4) or the predefined values shown in Fig. 6b (labelled MF), which

is thought to give a reasonable fit. Fig. 6a plots the velocities, Fig. 6b the corresponding accelerations along the track, and Fig. 6c shows the retarding acceleration vs. velocity. The parameters chosen for the VS-model are $\mu = 0.25$, $\xi = 2000$ m s^{-2}, and $h_a = 1.5$ m to give an overall fit. Using $\xi = 2000$ m s^{-2} deviates from the commonly used recommendations, which recommend ξ between ≈ 500–1000 m s^{-2}. The proposed values for μ are between 0.15 and 0.3 (cf. Buser and Frutiger, 1980; Gruber et al., 1999). Higher values for ξ makes the model less velocity dependent. Two things are evident for the VS approach. First, between −250 m and 0 m horizontal distance from the steel tower, the model overestimates the observed velocity and does not follow the significant deceleration–acceleration phase, which is observed (cf. Fig. 6b). This deceleration–acceleration behavior seems to be typical for the Ryggfonn path as it was observed in several other avalanche events, for example in the 19970417 14:00 event (cf. Gauer et al., 2007). That avalanches might show typical velocity behaviors due to the topography of their path was already mentioned by, e.g., Kotlyakov et al. (1977). Secondly, the VS-model does not come to a stop before it runs into the dam, i.e., using the above parameters the model overestimates the runout. The reason for this is the rather low friction coefficient, μ. The observed effective friction coefficient, μ_{eff}, is around 0.4–0.5. If one uses the parameters $\mu = 0.25$, $\xi = 1000$ m s^{-2}, and $h_a = 1.5$ m in the VS-model, which are close to the recommendations, the VS-model would fulfill two requirements: 1) the

calculated avalanche will surpass the bowl and 2) it will still come to stop in front of the dam. However, the velocity would be underestimated during most of the time. Still, the velocity would be overestimated in the final runout. In other words, due to the low friction coefficient, the length of the runout will be overestimated. The rather velocity independent retarding acceleration in

the case of the fit is in agreement with the presented radar measurements above and with radar measurements presented in Gauer et al. (2007). It is also in agreement with the observations made by Salm and Gubler (1985) as well as by Ancey and Meunier (2004). Actually, it seems that the retarding acceleration is also rather independent of the slope angle. This could be reasonable, if one assumes that
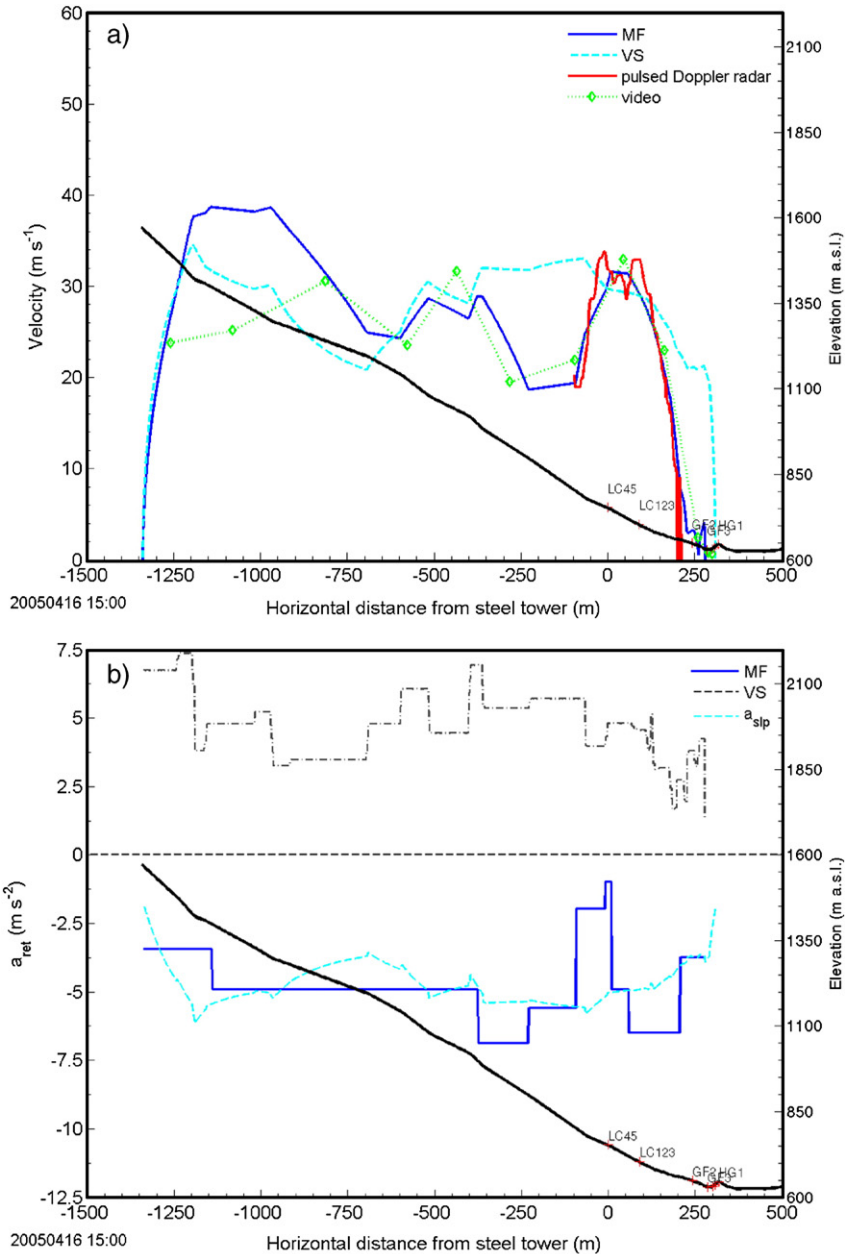

Fig. 6. Avalanche 20050416 15:00: a) estimated front velocity along the track based on video analysis and pulsed Doppler radar measurements. Note that the video analysis gives only mean values involving a degree of uncertainty along certain stretches. In addition the velocity evolution for two simple model calculations is shown. b) Corresponding retarding accelerations and the driving component of gravitational acceleration. c) Retarding acceleration vs. velocity. VS marks the Voellmy–Salm type and MF the "mass block fit".
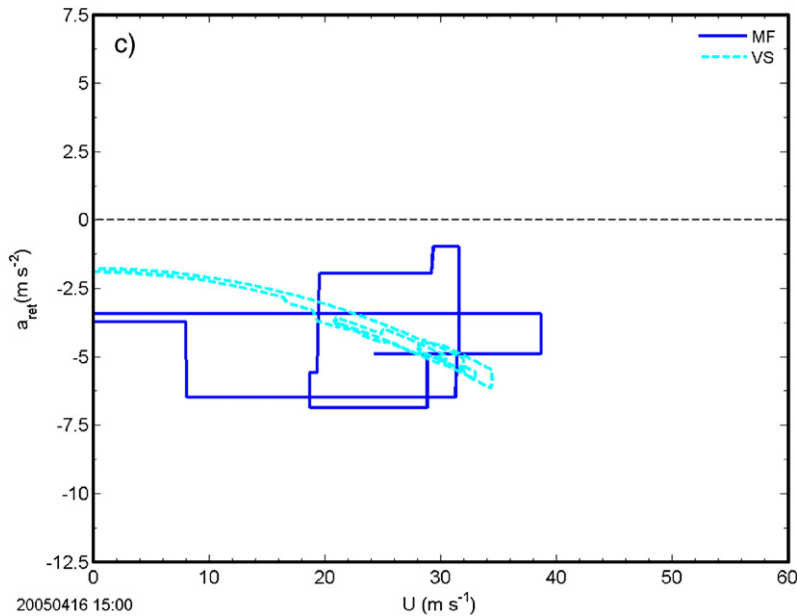
Fig. 6 (*continued*).

erosion or the development of a shear failure at the sliding plane (c.f. Section 3.3 and a similar one in Gauer et al. (2006)), the strength of the snow determines the retarding forces rather than a constant Coulomb friction coefficient. However, we cannot be conclusive on this point yet.

This analysis does not claim to give the full insight to avalanche dynamics. It is rather thought to pinpoint some of the problems, which we are facing in the understanding of the dynamics and that the classical models are considerably inappropriate. It should be noted that the VS-type model does usually not account for entrainment and its effect on the dynamic behavior. However, these models are still widely used for practical work since they are easy to handle.

3.2. Pressure measurements

The drag force, F_D, on a body submerged (or partly immersed) in a flow can be viewed as having two components: a pressure drag, F_p, and a friction drag, F_f (e.g., Franzini and Finnimore, 1997, Ch. 9). However, it is customary to express the total drag on a body by a single equation

$$F_D = C_D A \frac{\rho U_\infty^2}{2}. \tag{6}$$

This expression relates the drag force to the dynamic pressure $\rho U_\infty^2 / 2$, acting on the projected area, A, of the body normal to the flow. ρ is the density of the flow and U_∞ the flow velocity upstream of the body. It is well known in fluid mechanics that C_D depends on the geometry of the submerged body or the sensor configuration, respectively, and factors that define the behavior of the flow like the Reynolds number, Re, the Froude number, Fr, or possibly the Mach number, M. In addition, geometrical relations might be of importance, like obstacle geometry vs. particle size. In the case of a free surface flow, i.e., when the obstacle is only partly immersed, a fluid free zone, a "vacuum", can develop behind the obstacle. The depth and extent of this zone depends on the flow velocity and properties of the flow. In addition to the dynamic drag, an unbalanced static load is imparted onto the obstacle. This static load is also measured by sensors mounted to an obstacle and which are capable of measuring static loads; not all piezo-electric pressure sensor systems have long enough time constant to measure static loads. If one includes the static pressure acting on a sensor, the equation for the drag force actually takes on the following form

$$F_D = \left(C_D + \frac{f_s}{Fr_\infty^2} \right) A \frac{\rho U_\infty^2}{2} = C_D^* A \frac{\rho U_\infty^2}{2}, \tag{7}$$

where the Froude number, $Fr_\infty = U_\infty / \sqrt{g h_\infty}$; h_∞ is the upstream flow depth. It is reasonable to assume that the function f_s depends on the ratio between submerged depth and flow depth and on other factors. The contribution from the quasi-static component might become negligible for $Fr_\infty \gg 1$. However, if Fr_∞ drops below one, the quasi-static load may dominate the drag.

In the limit of very low velocity, Eq. (7) should predict the load because of snow creeping.

Fig. 7 shows the measured impact pressure and the corresponding radar (approach) velocity. Here, the position within the avalanche is a measure of distance behind the front as the avalanche passes the sensor (it is similar to the wind run used in meteorology). The measured pressures of up to 600–800 kPa are surprisingly high. These pressures are probably related to the damp or wet snow slide behaving like a cohesive flow with high shear strength, but could also be attributed to some large and hard snow blocks originating from the cornice, or a combination of both. At the front of the avalanche, we observe a fluidized (saltation) layer before the more dense part arrives. If one relates the measured pressure values, LC, with the
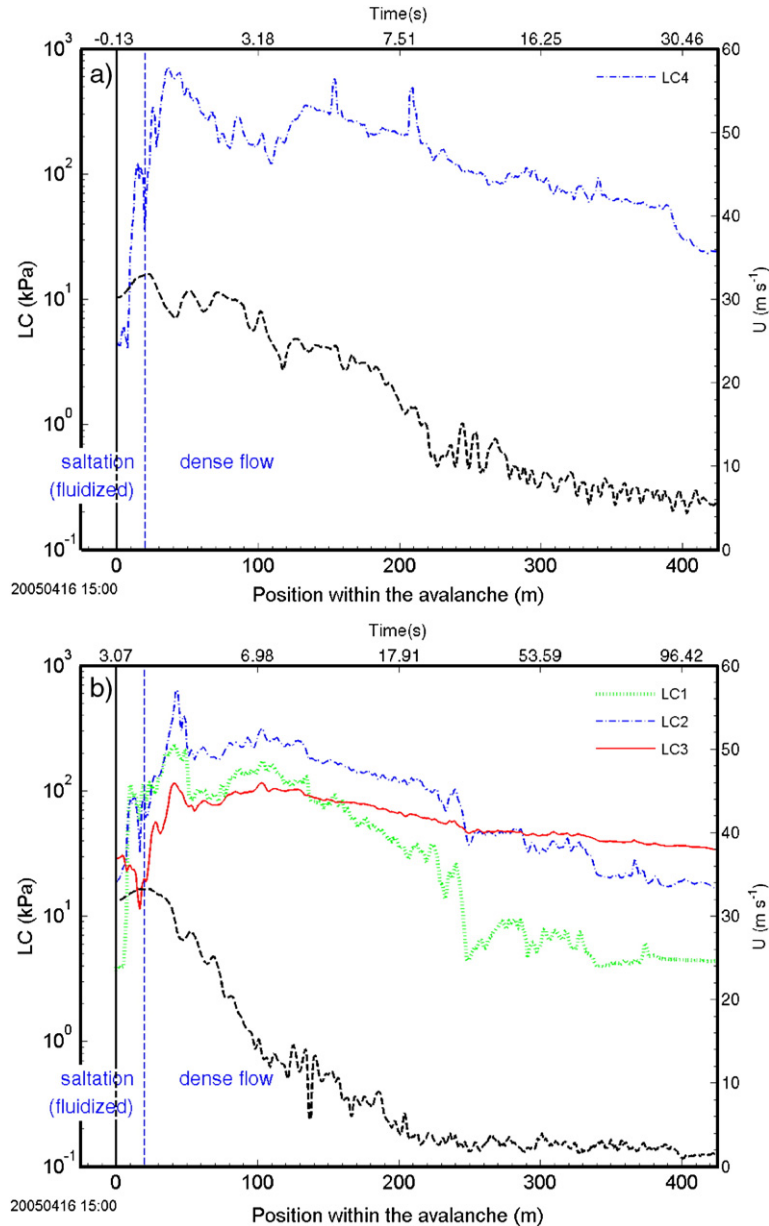

Fig. 7. Avalanche 20050416 15:00: pressure vs. position within the avalanche; a) load cell LC4 at the steel tower and b) load cells at the concrete wedge. Note the logarithmic scaling of the left ordinate. The time scale on top gives the corresponding time stamps. Values are running means with 5 m filter width. The black dashed lines show the corresponding velocity profiles (LC5, which is not shown here, was totally buried and initially, LC3 was partially buried).

dynamic pressure, one can gain an estimate of the combination of density and combined drag factor

$$\rho C_D^* = \frac{2LC}{A_e U^2},\tag{8}$$

where A_e is the effected sensor area and U the measured velocity. If one further assumes a density, ρ, between 300 and 500 kg m^{-3} within the slowly moving tail, one finds a C_D^* of approximately 20 to 40

for LC2 in the tail. Values that are typically proposed for C_D^* are in the range of 2–6 (cf. Norem, 1990; Salm et al., 1990; Mellor, 1968). The measurements indicate that the drag factor depends much more on the flow regime than is commonly recognized. Especially, the force in slow moving avalanches might be considerably underestimated using common values.

The dependency on the flow regime can be seen if one plots the measured pressure at the loads cell vs. velocity as
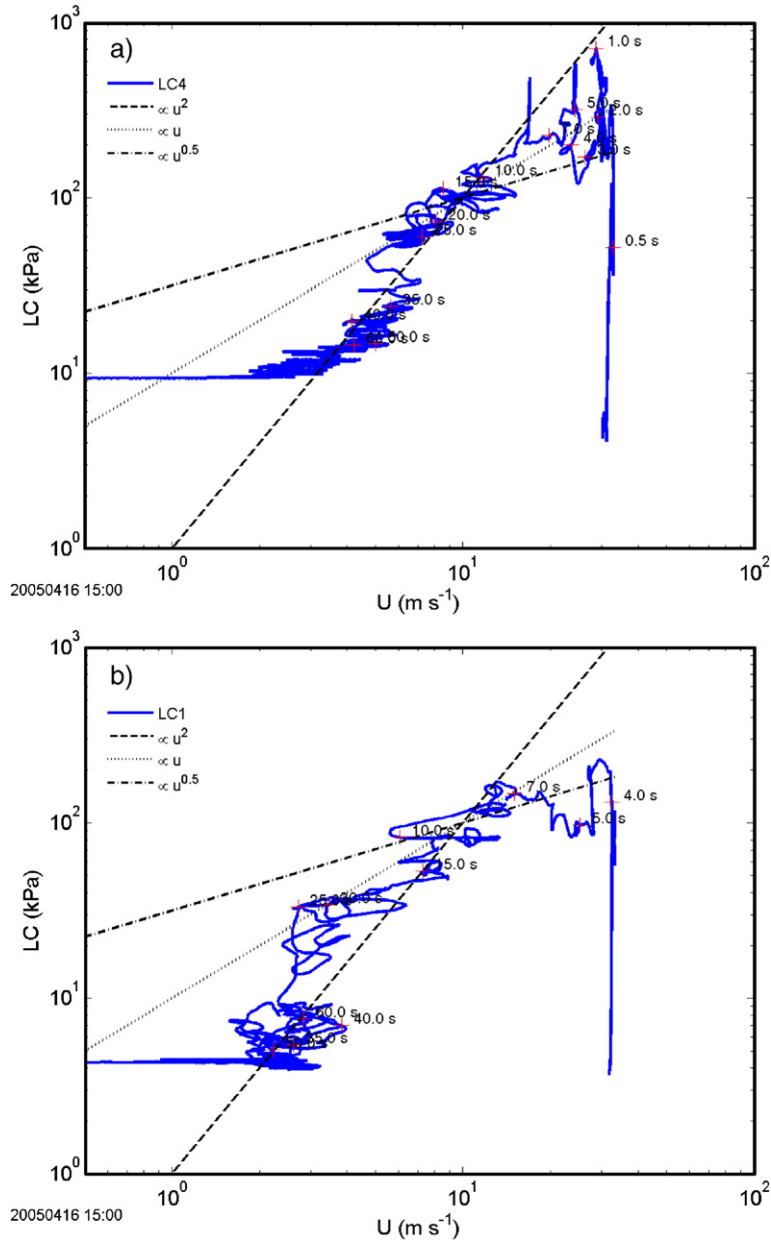

Fig. 8. Avalanche 20050416 15:00: pressure vs. velocity; a) load cell LC4 at the steel tower, b) LC1 at the concrete wedge and c) LC2 at the concrete wedge. Note the log–log scaling. Values are running means with 5 m filter width. The additional lines indicate different proportionalities and crosses mark time stamps relative to the arrival at the steel tower.
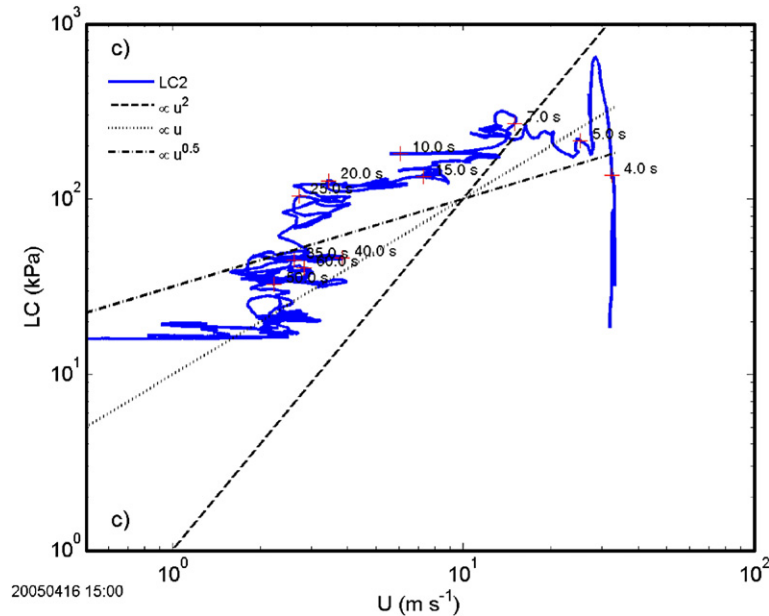
Fig. 8 (*continued*).

it is shown in Fig. 8 for LC4, LC1, and LC2. Vice versa, the measurements indicate transitions in the flow behavior (regime). The additional lines shown in the figure mark a proportionality to $\sqrt{U}$, U, and U^2, respectively. In all cases, we see a rapid, but not instantaneous, increase in the pressure by nearly constant velocity (see also Fig. 7). Thereafter, there appears to be a peak followed by a pressure drop. In the case of LC4, there is an interval (approximately between 2.1 to 3.5 s) in which the pressure follows $\propto U^2$, and then the pressure is rather $\propto U$. This transition probably indicates a transition in the flow behavior for this avalanche[1]. At the concrete wedge, we see that the upper sensor LC1 follows more a $\propto U$ behavior whereas the LC2 (and also LC3, which is not shown) seem to be $\propto \sqrt{U}$ for longer periods. This indicates that there is also a vertical variation in the flow behavior. However, it might also be an artifact due to flow height changes (or a combination of both). Issues such this need to be followed up in future experiments.

As there are no direct measurements on the flow density and flow height and the correct vertical velocity profile is unknown, we cannot quantitatively evaluate C_D^*. Nevertheless, if one assumes a self-similar velocity profile as a first approximation, the contribution from a vertical velocity profile to the variation of C_D^* would be an additional constant factor, but would not change the proportionality (power) dependency on U. Hence, we can observe spatial changes in the flow behavior as aforementioned.

Furthermore, there are also phases of transition where the measured pressure actually increases with decreasing velocity, which also indicates a transition in the flow, e.g., change in density, flow height, etc. In the tailing part pressure decreases while the velocity changes only a little, which indicates again a change in the flow behavior.

Due to the missing additional measurements (height, density, velocity profile, etc.) we cannot be conclusive. Although, we observed similar behavior in other avalanches for which we have pulsed Doppler radar data and pressure measurements are available. These are the 19970417 14:00 and 20030406 13:06 events, which are shown in Fig. 9.

The 19970417 14:00 avalanche was released by similar conditions as the 20050416 15:00 one, i.e., it started as a dry-mixed avalanche and ran into damp snow in the valley bottom. A plot of the pressure scaled by U^2 vs. position within the avalanche can be found in (Gauer et al., 2006). In Fig. 9, it can be seen that pressure evolution shows two periods with $\propto U^2$ that are connected by a period of more or less constant pressure during decreasing velocity. Again this might be caused by a change of the density and/or flow height. In the tailing part the dependency switches to $\propto U$. Here, we only show the data from LC2. However,

---

[1] For example, in viscous flows, like mud-flows, a change from $p \propto U^2$ to $p \propto U$ or even a velocity independency can be expected when Reynolds number of the flow drops below a certain value. In the case of mud-flows the Reynolds number might be defined by $Re = \rho U_\infty^2 / Y$, where Y is the yield stress of the mud and the transition starts at approximately $Re < 100$ (Gauer and Kvalstad, unpublished).
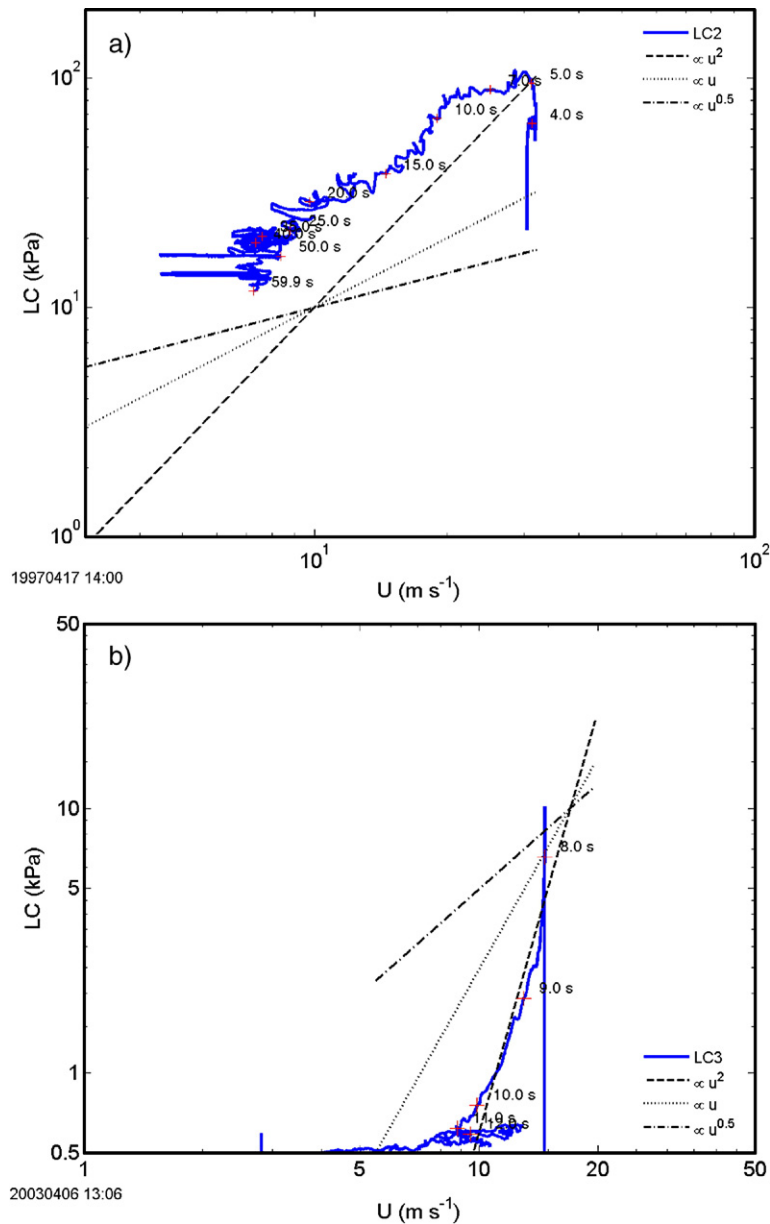
Fig. 9. Pressure vs. velocity; a) avalanche 19970417 14:00, sensor LC2, b) 20030406 13:00, sensor LC3. Note the log–log scaling. The additional lines indicate different proportionalities and crosses mark time stamps relative to the arrival at the steel tower. Both measurements originate from the concrete wedge.

LC3 also had qualitatively a similar behavior despite it was probably partly buried. No data are available for LC1.

The 20030406 13:06 avalanche was a small dry-mixed one, which shortly below the concrete wedge came to a stop. Video footage implies that the front was rather fluidized although the velocities were rather low. After impact, the pressure decreases as $\propto U^2$ in this case.

In all cases above, one can see a rapid, but not instantaneous increase of the pressure by nearly constant velocity at time of arrival. This increase is probably related to an increase in density and accompanies the transition from a more fluidized to a more dense flow. This can also be seen from Fig. 10.

Having the impact pressure $\propto U^n$, where n typically ranges from 0 to 2, it follows from Eq. (8) that ρC_D^* is $\propto U^{n-2}$. Fig. 10 shows example plots of this relation for the events 19970417 14:00 and 20050416 15:00. It is reasonable to assume that the density within the

dense part of an avalanche is rather constant. The change is probably not more then a factor of 2–3, so that the major part of the changes seen in the figure can be attributed to changes in C_D. Although both events were thought to be released under similar conditions we notice a considerable difference between the ρC_D curves.

3.3. Load plate measurements

Fig. 11 presents measurements from the load plate LP1 in the dam slope. It shows the total traction, Q, vs. the normal pressure, P, at the sliding surface (boundary between snowpack including deposits of previous events and avalanche).
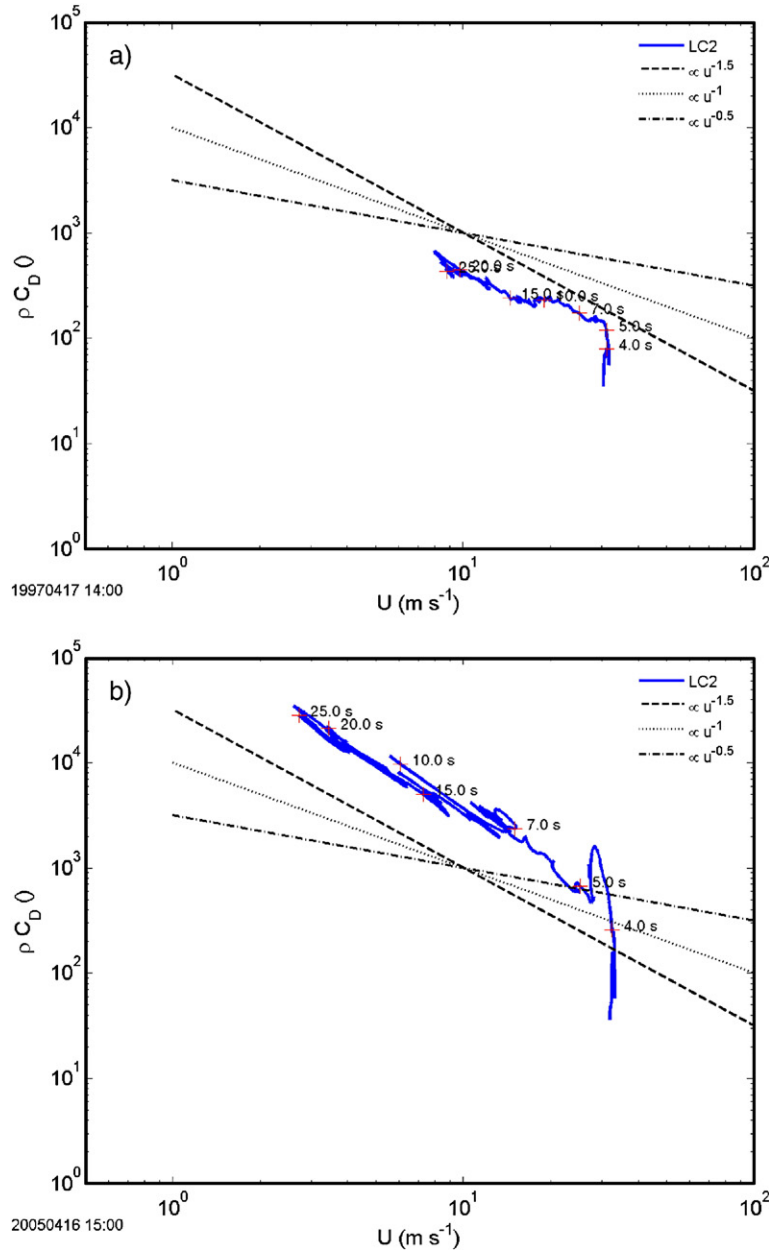

Fig. 10. ρC_D vs. velocity; a) avalanche 19970417 14:00, sensor LC2, b) 20050416 15:00, sensor LC2. Note the log–log scaling. The additional lines indicate different proportionalities and crosses mark time stamps relative to the arrival at the steel tower. Both load cell measurements originate from the concrete wedge.
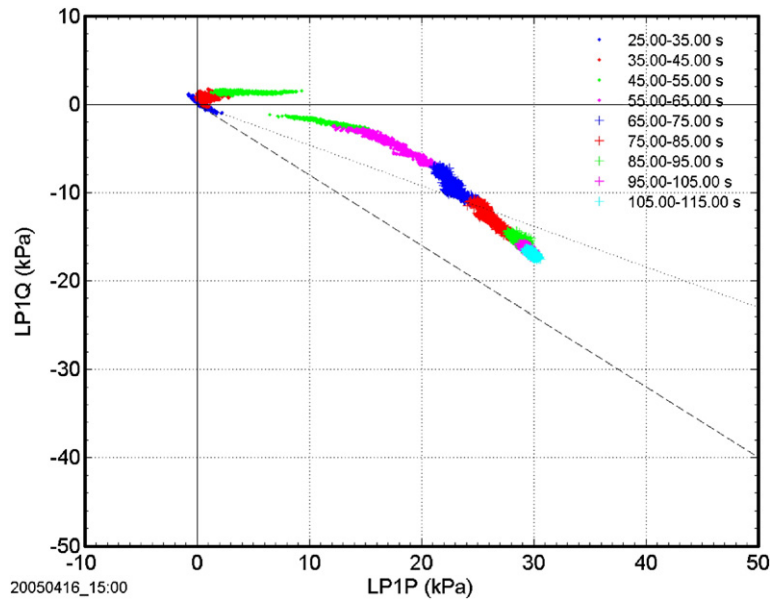
Fig. 11. Avalanche 20050416 15:00: load plate measurements: shear stress vs. normal stress at the sliding plane (surface of the snowpack) along the dam slope. Shown is the lower plate LP1. Q is the total traction and P the normal stress at the sliding plane. The dashed line in the panel corresponds to the ratio between shear and normal stress in the case of static loading ($-\tan 40°$ or $-\tan 20°$).

To gain the stresses at the sliding surface, the stresses measured at the load plate need to be related to the sliding surface.

$$P = f_p\left(LP_z, LP_x, LP_y, \alpha\right),$$
$$Q = f_q\left(LP_z, LP_x, LP_y, \alpha\right), \tag{9}$$

where LP_z, LP_x, and LP_y are the measured forces in z-, x-, and y-direction, respectively, at the load plate; α is the angle between the sliding surface and the plane of the load plate. The functions f_p and f_q might be approximated by superposing the Boussinesq solutions for point loads normal and tangential to the contact surface with an elastic, isotropic and semi-infinite medium and integrating them over the loaded area. To this end, it is necessary to have information above the snow deposit in the surrounding of the load plate prior to the event. For a

Fig. 12. Avalanche 20050416 15:00: snapshot of the deposits. The arrow indicates the approximate location of the load plate, however the main deposit is slightly off side of the plate (photo by Arne Moe/NGI).
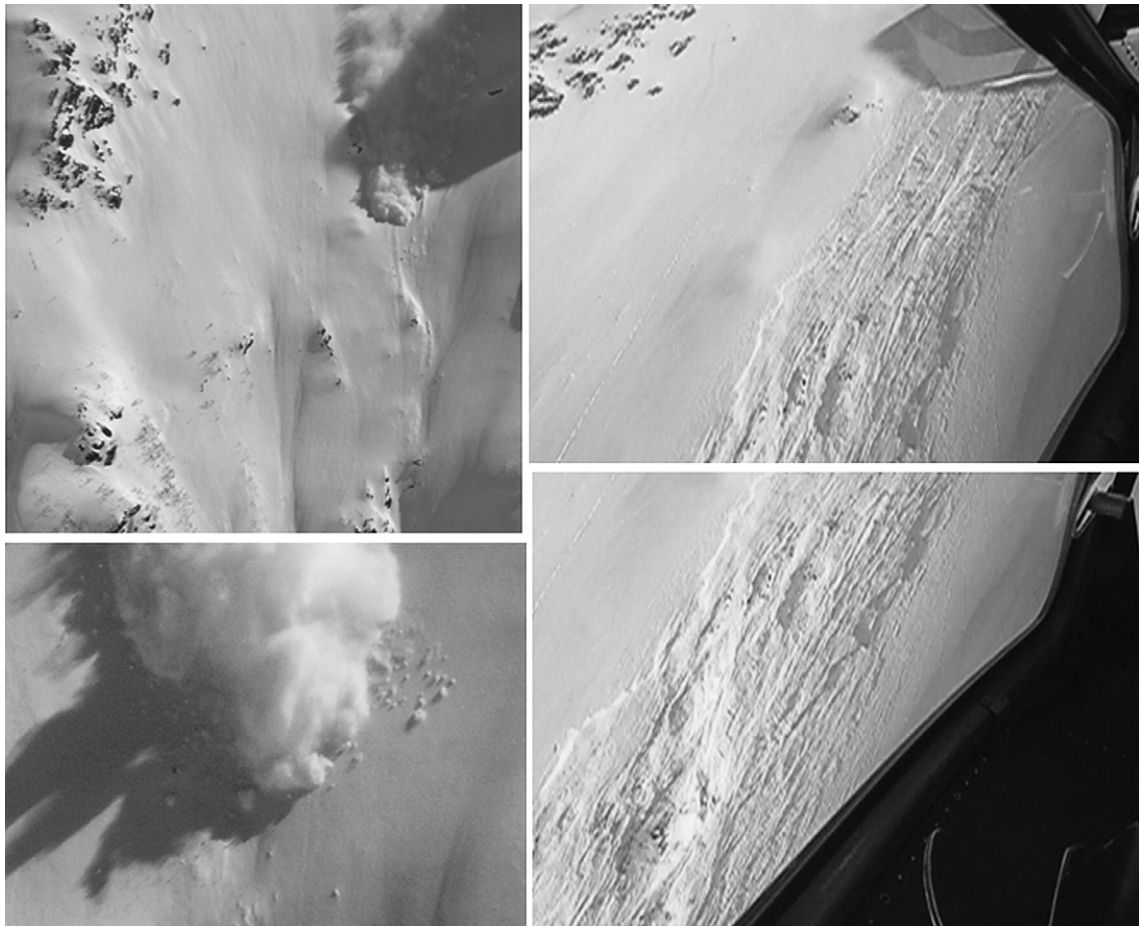
Fig. 13. Avalanche 20050416 15:00: snapshots of the track; left hand side, during the descent of the avalanche; right hand side after the event (similar location). Obviously, the avalanche eroded during the descent. Scratch marks remind one at erosion/abrasion due to (saltating) particles (photos by Arne Moe/NGI).

detailed explanation of how the measurements at the load plates can be related to the sliding surface, we refer to Gauer et al. (2006).

Only the slow moving wet part arrived at the dam and slowly loaded the load plate. On arrival of the avalanche, the shear stress increases with the normal stress ($t = 35$–45 s). Then, a shear (plastic) failure is obvious ($t = 45$–55 s), i.e., the shear stress is independent of the normal stress. In this case, the yield stress is about 1.5–2 kPa. Thereafter, the plot basically shows a static loading in which case one would expect $Q/P = -\tan \phi_e$, where ϕ_e is the effective slope angle. The dam slope is about 40°, the slope of the deposit in front of the dam prior to the event was about 20°. To give an impression of the final stage, Fig. 12 depicts a snapshot of the deposit. The height over the load plate is about 8 m of fresh deposit.

3.4. Erosion

One of the puzzling questions, which was disregarded for awhile after first descriptions by various authors such as Grigorian and Ostroumov (1977), Eglit (1983), Brugnot and Pochat (1981), Mellor (1968), Hopfinger and Tochon-Danguy (1977), but recently regained attention (Sovilla et al., 2001; Sovilla, 2004; Sovilla et al., 2006), is the question of mass balance and erosion mechanisms. Gauer and Issler (2004) proposed several possibilities, among others erosion/abrasion due to (saltating) particles. Fig. 13 shows snapshots from the track during and after the avalanche descent at about the same location. The erosion of the snowpack by the avalanche is obvious. The scratch marks remind one at abrasion due to particles or clods.

The initial volume of the avalanche was about $10–15 \cdot 10^3$ m^3 (approximately $4–6 \cdot 10^6$ kg). In addition, it triggered a secondary wet slide in the lower part of the track, with approximately $5–10 \cdot 10^3$ m^3 (approximately $2–4 \cdot 10^6$ kg). The deposit was around $80 \cdot 10^3$ m^3. The difference suggests that the avalanche eroded on average about 0.1 to 0.2 m/m^2 along its way down, which is in accordance with the field observations.

4. Discussion and conclusions

Measurements and field observations are presented on an artificially released avalanche at the Norwegian full-scale avalanche test-site.

Velocity measurements using pulsed Doppler radar and deduced retarding acceleration imply that friction terms in classic avalanche models (for example Salm et al. (1990), Perla et al. (1980)) overestimate the resistance at high avalanche speeds and underestimate it in the runout phase. This has consequences for hazard zoning.

Pressure measurements with large size load plates suggest that drag factors in the slow moving wet parts of an avalanche can reach values of 20 to 40, which is far more than what is commonly used. With even such basic things as the drag coefficient not yet understood, there is much more research that need to be undertaken in this area. Some preliminary discussions on C_D values relevant for avalanches can be found in (Gauer et al., 2006; Eglit et al., in press) and references therein. The presentation of the pressure measurements vs. flow velocity strongly implies the existence of different flow regimes within the avalanche. These flow regime transitions need to be further studied to improve numerical models.

Field observations (scratch marks in the remaining snowpack along parts of the track and video analysis) from the avalanche event indicate that substantial entrainment occurred and that erosion/abrasion due to saltating and sliding particles is a possible mechanism (cf. Gauer and Issler, 2004). However, there is definitely more work to be done to obtain a better understanding of the mass balance and the involved mechanisms.

Still, further work is needed to combine results from different sensors to construct a clearer picture of the avalanche structure. At the Ryggfonn site, we hope, for example, to gain some further insight from the FMCW-radars in the next years. In addition, as some of the observations might be specific to the avalanche path, it is important to cross-check results from Ryggfonn with measurements from other test-sites.

References

Ammann, W.J., 1999. A new Swiss test-site for avalanche experiments in the Vallée de la Sionne/Valais. Cold Regions Science and Technology 30 (1–3), 2–11.

Ancey, C., Meunier, M., 2004. Estimating bulk rheological properties of flowing snow avalanches from field data. Journal of Geophysical Research 109 (F01004). doi:10.1029/2003JF000036.

Bakkehøi, S., Domaas, U., Lied, K., 1983. Calculations of snow avalanche runout distance. Annals of Glaciology 4, 24–28.

Barbolini, M., Issler, D., 2006. Avalanche test sites and research equipment in Europe: an updated overview. Final-Report Deliverable D8. SATSIE Avalanche Studies and Model Validation in Europe.

Bozhinskiy, A.N., Losev, K.S., 1998. The fundamentals of avalanche science. Mitt. Eidgenoss. Inst. Schnee- Lawinenforsch. 55. EISLF Flüelastr 11. CH-7260 Davos. Mitt. Eidgenöss. Inst. Schnee-Lawinenforsch, Davos.

Brugnot, G., Pochat, R., 1981. Numerical simulation study of avalanches. Journal of Glaciology 27, 77–88.

Buser, O., Frutiger, H., 1980. Observed maximum run-out distance of snow avalanches and the determination of the friction coefficients μ and ξ. Journal of Glaciology 26 (94), 121–130.

Eglit, E.M., 1983. Some mathematical models of snow avalanches, In: Shahinpoor, M. (Ed.), 1st edition. Advances in the Mechanics and the Flow of Granular Materials, vol. II. Trans Tech Publications, Clausthal-Zellerfeld, Germany, pp. 577–588.

Eglit, M.E., Kulibaba, V.S., Naaim, M., in press. Impact of a snow avalanche against an obstacle. Formation of shock waves. Cold Region Science and Technology.

Franzini, J.B., Finnimore, Jo.E., 1997. Fluid Mechanics with Engineering Applications. McGraw-Hill.

Gauer, P., Issler, D., 2004. Possible erosion mechanisms in snow avalanches. Annals of Glaciology 38, 384–392.

Gauer, P., Kristensen, K., 2004. Avalanche Studies and Model Validation in Europe, SATSIE: Ryggfonn Measurements Winter 2002/2003 and 2003/2004. NGI Report 20021048-5. Sognsveien 72, N-0806 Oslo. Norwegian Geotechnical Institute.

Gauer, P., Kristensen, K., 2005. Avalanche Studies and Model Validation in Europe, SATSIE: Ryggfonn Measurements Winter 2004/2005. NGI Report 20021048-8. Sognsveien 72, N-0806 Oslo. Norwegian Geotechnical Institute.

Gauer, P., Kvalstad, T., unpublished.

Gauer, P., Issler, D., Lied, K., Kristensen, K., Iwe, H., Lied, E., Rammer, L., Schreiber, H., 2006. On full-scale avalanche measurements at the Ryggfonn test site, Norway. Cold Region Science and Technology. doi:10.1016/j.coldregions.2006.09.010.

Gauer, P., Kern, M., Kristensen, K., Lied, K., Rammer, L., Schreiber, H., 2007. On pulsed Doppler radar measurements of avalanches and their implication to avalanche dynamics. Cold Region Science and Technology. doi:10.1016/j.coldregions.2007.03.009.

Grigorian, S.S., Ostroumov, A.V., 1977. Matematicheskaya model sklonovih processov lavinnogo tipa [The Mathematical Model for Slope Processes of Avalanche Type] (in Russian). Scientific Report 1955. Institute for Mechanics, Moscow State University, Moscow, Russia.

Gruber, U., Bartelt, P., Margreth, S., 1999. Neue Berechnungsmethoden in der Lawinengefahrenkartierung. Technical Report Part III. Flüelastr. 11, CH-7260 Davos-Dorf, Eidgenöss. Inst. Schnee- und Lawinenforsch.

Gubler, H.-U., 1987. Measurements and modelling of snow avalanche speeds. In: Salm, B., Gubler, H.-U. (Eds.), Avalanche Formation, Movement and Effects, vol. 162. IAHS Publ., pp. 405–420.

Hopfinger, E.J., Tochon-Danguy, J.-C., 1977. A model study of powder-snow avalanches. Journal of Glaciology 19 (81), 343–356.

Issler, D., 1999. European avalanche test sites: overview and analysis in view of coordinated experiments. Mitteilungen 59. Flüelastr 11. CH-7260 Davos. Eidgenöss. Inst. Schnee- Lawinenforsch, Davos.

Issler, D., 2003. Experimental information on the dynamics of dry-snow avalanches. In: Hutter, K., Kirchner, N. (Eds.), Dynamic Response of Granular Materials under Large and Catastrophic Deformations, Volume 11 of Lecture Notes in Applied and Computational Mechanics. Springer, pp. 109–160.

Kawada, K., Nishimura, K., Maeno, N., 1989. Experimental studies on a powder-snow avalanche. Annals of Glaciology 13, 129–134.

Kotlyakov, V.M., Rzhevskiy, B.N., Samoylov, V.A., 1977. The dynamics of avalanching in the Khibins. Journal of Glaciology 19 (81), 431–439.

McClung, D.M., Schaerer, P.A., 1985. Characteristics of flowing snow and avalanche impact pressures. Annals of Glaciology 6, 9–14.

McClung, D., Schaerer, P., 1993. The Avalanche Handbook. (1011 SW Klickitat Way), Seattle, Washington 98134. The Mountaineers, USA.

Mellor, M., 1968. Cold regions science and engineering. Part III: Engineering, Section A3: Snow Technology Avalanches. Cold Regions Research & EngineeringLaboratory, Hanover, New Hampshire.

Nishimura, K., Narita, H., Maeno, N., Kawada, K., 1989. The internal structure of powder-snow avalanches. Annals of Glaciology 13, 207–210.

Nishimura, K., Maeno, N., Kawada, K., Izumi, K., 1993. Structures of snow cloud in dry-snow avalanches. Annals of Glaciology 18, 173–178.

Norem, H., 1990. Ryggfonn-prosjektet. NGI Report 581200-16. Sognsveien 72, N-0806 Oslo. Norwegian Geotechnical Institute. (in Norwegian).

Norem, H., Kvisterøy, T.K., Evensen, B.D., 1985. Measurements of avalanche speeds and forces: instrumentation and preliminary results of the Ryggfonn project. Annals of Glaciology 6, 19–22.

Perla, R., Cheng, T.T., McClung, D.M., 1980. A two-parameter model of snow-avalanche motion. Journal of Glaciology 26 (94), 197–207.

Rammer, L., Kristensen, K., Lied, K., Schreiber, H., Randeu, W., 1998. Radar measurements of snow avalanche full scale experiment in Ryggfonn. In: Hestnes, E. (Ed.), 25 Years of Snow Avalanche Research, (NGI Publ. 203). Norwegian Geotechnical Institute, Oslo, pp. 268–273.

Salm, B., Gubler, H., 1985. Measurement and analysis of the motion of dense flow avalanches. Annals of Glaciology 6, 26–34.

Salm, B., Burkard, A., Gubler, H.U., 1990. Berechnung von Fliesslawinen. Eine Anleitung fur Praktiker mit Beispielen. Mitt. Eidgenöss. Inst. Schnee- Lawinenforsch. 47. SLF, Davos, Switzerland, p. 37.

Schaerer, P.A., Salway, A.A., 1980. Seismic and impact–pressure monitoring of flowing avalanches. Journal of Glaciology 26 (94), 179–187.

Schreiber, H., Randeu, W.L., Schaffhauser, H., Rammer, L., 2001. Avalanche dynamics measurement by pulsed Doppler radar. Annals of Glaciology 32, 275–280.

Sovilla, B., 2004. Field Experiments and Numerical Modelling of Mass Entrainment and Deposition Processes in Snow Avalanches. Ph.d thesis, ETH Zurich.

Sovilla, B., Sommavilla, F., Tomaselli, A., 2001. Measurements of mass balance in dense snow avalanche events. Annals of Glaciology 32, 230–236.

Sovilla, B., Burlando, P., Bartelt, P., 2006. Field experiments and numerical modeling of mass entrainment in snow avalanches. Journal of Geophysical Research 111, 1–16. doi:10.1029/2005JF000391F03007.

UNESCO, 1981. Avalanche Atlas. International Commission on Snow and Ice of the International Association of Hydrological Sciences. IAHS.